Supplementary materials

Laser induced white emission of Sr_2CeO_4 nanocrystals

W. Strek [a], R. Tomala [a]*, L. Marciniak [a], M. Lukaszewicz [a],

B. Cichy [a], M. Stefanski, D. Hreniak [a], A. Kedziorski [b], M. Krosnicki [c] and L. Seijo [d]

[a] *Institute for Low Temperature and Structure Research, Polish Academy of Sciences, Wroclaw, Poland*

[b] *Institute of Physics, Faculty of Physics, Astronomy and Informatics, Nicolaus Copernicus University, Toruń, Poland*

[c] *Institute of Theoretical Physics and Astrophysics, University of Gdańsk, Poland*

[d] *Departamento de Quimica, Instituto Universitario de Ciencia de Materiales Nicolás Cabrera, and Condensed Matter Physics Center (IFIMAC), Universidad Autónoma de Madrid, Spain*

*corresponding author: r.tomala@int.pan.wroc.pl

1. Calculating of laser spot size

The area of laser spot in focal point was measured using a method presented by Saleh [1], where the diameter of the focused spot is given by:

$$W_0' = \frac{2f\lambda}{\pi D} \quad (1)$$

where f is the focal length of lens, λ is the wavelength of the laser and D is the beam diameter. Thus, the area of a laser beam is:

$$A = \pi(\frac{1}{2}W_0')^2 \quad (2)$$

The spot diameters in intermediate points were calculated using the cone method.

2. Pressure dependence of LIWE intensity

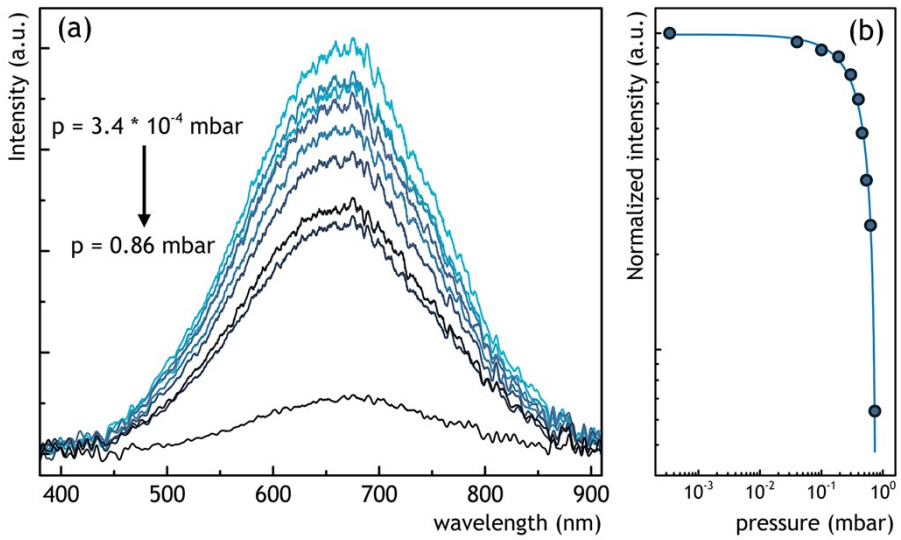

Figure S1. Pressure dependence of LIWE of Sr_2CeO_4 nanocrystals under 975 nm (7000 W/cm^2) (a,b) excitation.

3.Power dependence of pressure parameter p_o

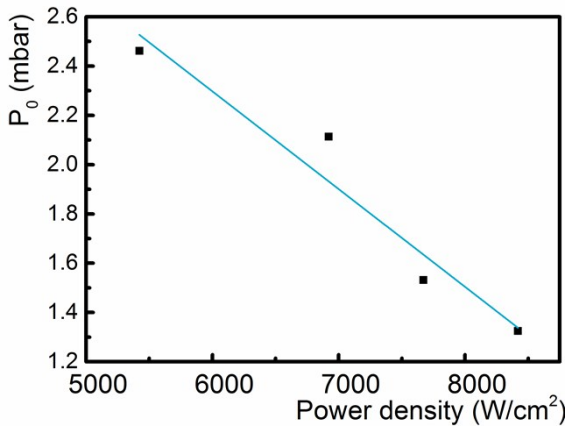

Figure S2. The dependence p_0 parameter on excitation density power.

3. Temperature of LIWE

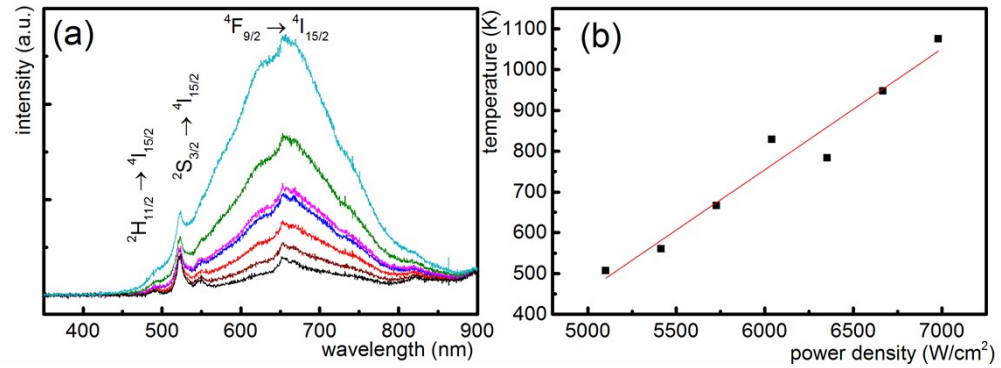

Figure S3. The emission spectrum of Sr_2CeO_4 + $LiYbP_4O_{12}$:Er^{3+} nanothermometer under different power of excitation beam of CW 975 nm laser (a); an influence of excitation power on temperature of white emitting sample (b).

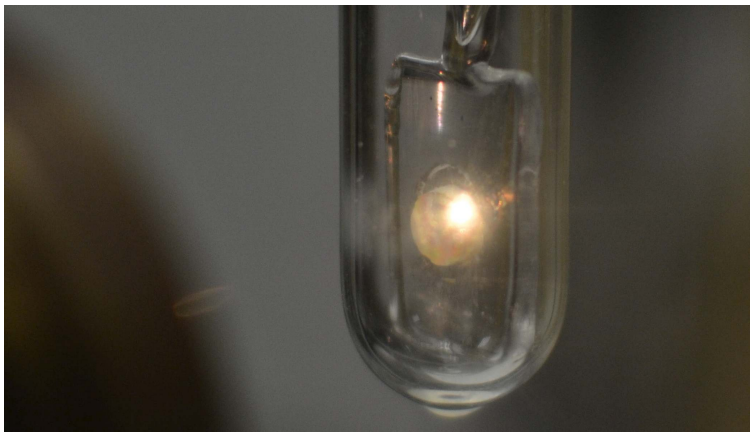

Figure S4. The picture of Sr_2CeO_4 emission under 975 nm laser diode excitation

4. The rise up and decay times

The influence of pumping power on rise time is shown in Fig 5a and 5c. The rise time decreases linearly with pump power.

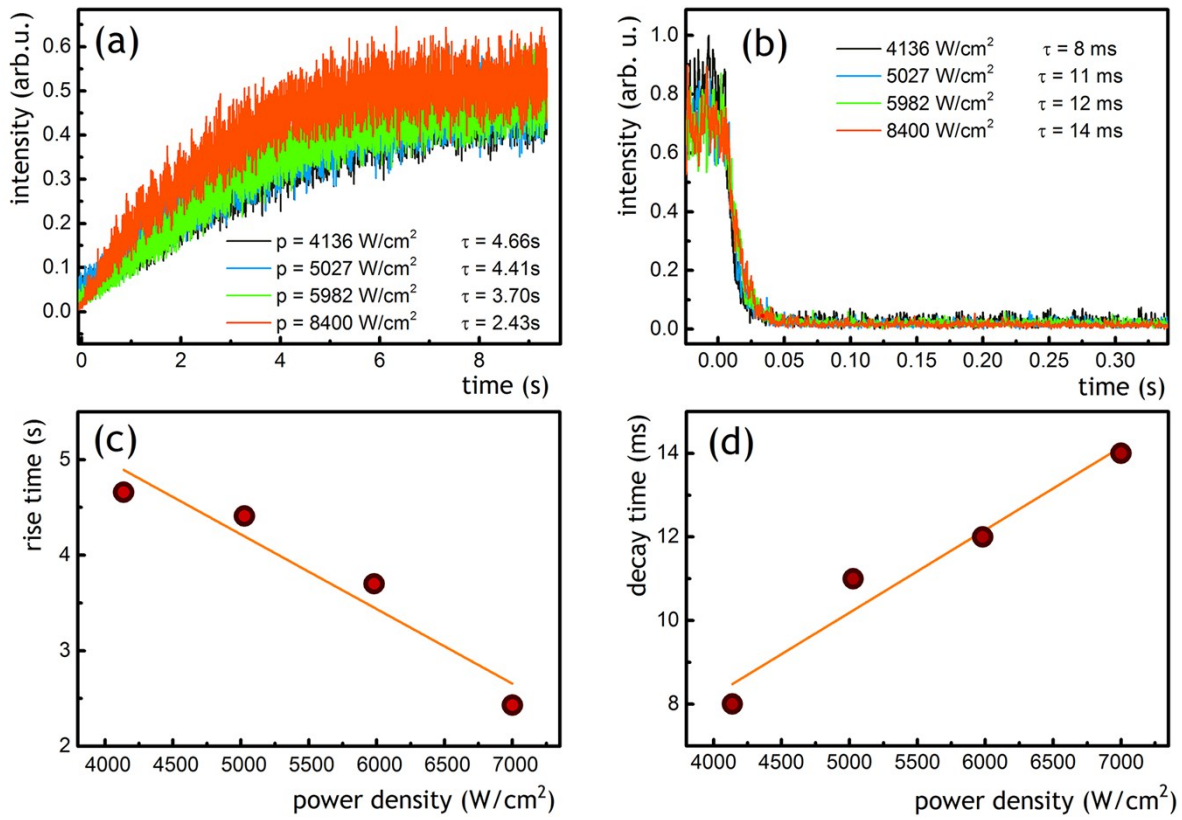

Figure S5. The kinetics of LIWE of Sr_2CeO_4. Dependence of the rise time (a,c) and decay times (b,d) on the excitation pumping power.

Figure 5b and 5d show a decay times of white emission. The decay time increases along with increasing the power density of 975 nm excitation.

S5. Model of IVCT transitions in Sr_2CeO_4

Assuming that the spectroscopic properties of Sr_2CeO_4 crystal are due to the independent Ce centers, thus the minimal theoretical treatment demands consideration of the $(CeO_6)^{8-}$ clusters embedded in Sr_2CeO_4 lattice. Within such cluster it is possible, in principle, to consider the LMCT states, in which the electron occupying the O 2p states is transferred to 4f state of Ce ion (Fig. S6). The transitions involving LMCT states are supposed to be responsible for the absorption and Stokes emission spectra of Sr_2CeO_4 crystals. In order to construct the

coordination diagram in the Fig.8, the explicit form of the vibrational normal modes, usually of the breathing mode[2] and its frequency, the positions of energy minima of the ground and excited states have to be known.

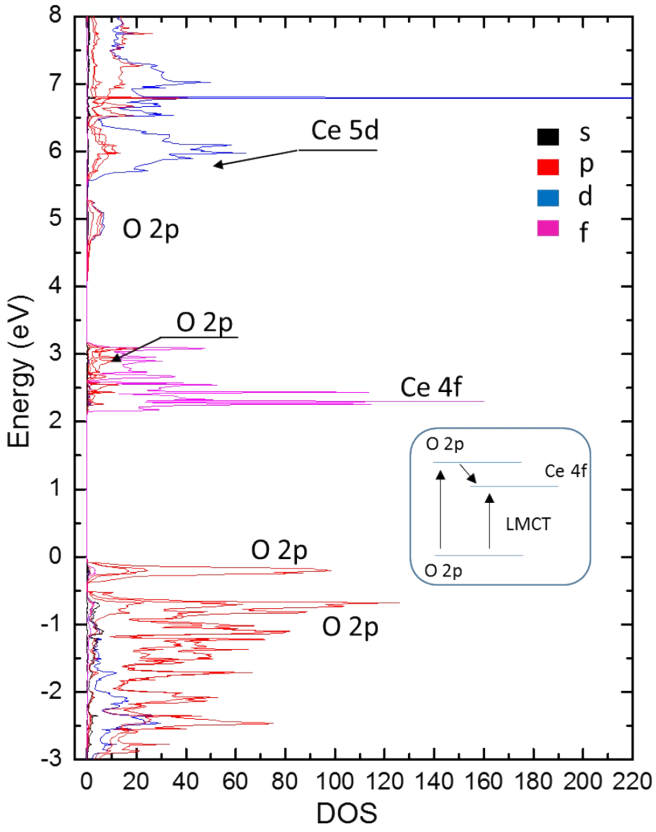

Fig. S6 Local density of states calculated for the Sr_2CeO_4 crystal. The valence band edge is composed mainly of the O 2p states as well as the first conduction bands.

Contrary to the highly symmetric sites of O_h symmetry, where the structural distortions of breathing mode are known *a priori*, the form of breathing mode of $(CeO_6)^{8-}$ embedded cluster site of C_{2h} symmetry has to be calculated explicitly. Thus, the ground state geometry of the $(CeO_6)^{8-}$ embedded cluster was optimized and the frequencies of the vibrational normal modes of the cluster were calculated within SCF (self-consistent field) and MP2 (second-order Moeller-Plesset perturbation theory) approaches. The energy curves of the ground and excited states were calculated for the $(CeO_6)^{8-}$ and $(CeO_6)^{9-}$ embedded clusters representing the Ce^{4+} and Ce^{3+} centers, respectively. The calculations were performed within quasi-relativistic approach allowing for inclusion of scalar relativistic effects as well as the spin-orbit orbit interaction. As the first step the multi-configurational SCF calculations were performed for both embedded clusters allowing for the inclusion of dynamical correlation effects originating from the open-shell character of the majority of the considered states. In the case of $(CeO_6)^{8-}$ cluster the calculations were performed within RASSCF approach (Restricted Active Space SCF)

allowing for single excitations from O 2p states into the 4f and three low-lying 5d states of Ce ion. At the same time, the CASSCF approach (Complete Active Space SCF) was applied for the $(CeO_6)^{9-}$ embedded cluster allowing for calculation of the states of $4f^1$, $5d^1$ and $6s^1$ configurations of Ce^{3+} ion. The dynamic correlation effects were included here by means of second-order perturbation theory performed for RAS or CAS multi-reference wavefunctions for the $(CeO_6)^{8-}$ and $(CeO_6)^{9-}$ embedded clusters, respectively. Due to the fact that the calculations were performed with relatively small atomic basis set (of double-zeta quality) only the rather limited part of the dynamic correlation effects were taken into account here. Finally, the spin-orbit interaction was included within RASSI method (Restricted Active Space State Interaction). The energy curves for the ground and excited states of both embedded clusters were calculated along the breathing mode obtained for SCF method. As the result, the positions of the energy minima and the corresponding vibrational frequencies were extracted from the *ab initio* energy curves. Direct comparison of the geometry and vibrational frequencies with experiment is possible for the ground state of $(CeO_6)^{8-}$ embedded cluster representing Ce^{4+} site. Theoretical value of the average Ce-O bond lengths is 1.02(1.03) times smaller than the experimental one in the case of SCF (MP2) geometry optimization.

The application of the standard SCF scaling factor 0.817[3] of frequencies to the theoretical values of the breathing mode frequency of $(CeO_6)^{8-}$ embedded cluster results in the following frequencies 577 cm^{-1} (SCF), 568 cm^{-1} (MP2) that are close to the experimental value of 561 cm^{-1}. Taking into account the rather limited size of the atomic basis set and possibly minimal size of the cluster used in present calculations such discrepancies are expected. Furthermore, assuming that all the results of present ab initio calculations differ from the experimental counterparts in a systematic way, both scaling factors, 1.02 for Ce-O bond-lengths and 0.817 for vibrational frequencies were adopted here for all the considered states. In the Table 1 the minimum-to-minimum energies T_e, average Ce-O equilibrium bond-lengths R_e and vibrational frequencies $\hbar\omega$ of $(CeO_6)^{9-}$ embedded cluster obtained within *ab initio* calculations are presented; the values of R_e and $\hbar\omega$ are scaled as it is mentioned above. In particular, it is seen that the average frequency of breathing mode of $(CeO_6)^{9-}$ embedded cluster is smaller than that observed for Ce^{4+} center and equal to 515 cm^{-1}.

Table 1. Minimum-to-minimum energies T_e, average Ce-O equilibrium bond-lengths R_e and vibrational frequencies $\hbar\omega$ of $(CeO_6)^{9-}$ embedded cluster obtained within ab initio calculations. The theoretical values of Re and $\hbar\omega$ are scaled by 1.02 and 0.817 factors, respectively. Considered here 5d states are of approximate t_{2g} character corresponding to ideal octahedron CeO_6.

	R_e (Å)	T_e (cm^{-1})	$\hbar\omega$ (cm^{-1})
$4f^1\ {}^2F_{5/2}$	2.384	0	515
	2.384	0	515
	2.386	1148	516
	2.386	1148	516
	2.386	1604	516
	2.386	1604	516
$4f^1\ {}^2F_{7/2}$	2.384	2440	516
	2.384	2440	516
	2.387	3585	516
	2.387	3585	516
	2.387	4013	516
	2.387	4013	516
	2.388	4802	516
	2.388	4802	516
$5d^1$ 2D("t_{2g}")	2.372	22845	511
	2.372	22845	511
	2.376	26561	515
	2.376	26561	515
	2.380	27849	516
	2.380	27849	516

The (effective) vibrational normal mode 539 cm^{-1} that corresponds to the average value of force constants, $(k_{Ce4+}+k_{Ce3+})/2$. From the point of present discussion the most important feature of the configurational coordinate diagram that depends on vibrational frequency is the height of energy barrier that occurs between the minimum of the lowest $Ce^{3+}(5d^1)$ – Ce^{4+}(GS) state (GS denotes ground state) and the crossing point between this state and the highest IVCT $Ce^{3+}(4f^1)$ – Ce^{4+}(GS) state denoted by dashed lines in the Fig. 8. The value of this energy barrier is equal to 2500, 3400 and 4400 cm^{-1} for the vibrational frequencies 561, 539 and 515 cm^{-1}, respectively. The two extreme values 515 and 561 cm^{-1} correspond to the frequency of the breathing modes of Ce^{3+} and Ce^{4+} centers, respectively. The energy ranges of $4f^1$ and $5d^1$ states of Ce^{3+} ion denoted in the Fig. 8 are based on the *ab initio* energies T_e and scaled theoretical Ce-O bond-lengths R_e collected in the Table 1. Finally, it should be pointed out that the O(2p) → Ce(4f) LMCT states are not included in the Fig. 8. According to the present ab initio calculations performed for $(CeO_6)^{8-}$ embedded cluster the equilibrium Ce-O bond-lengths for LMCT state

are only slightly shorter (by a few 0.01 Å) than those for Ce^{3+}-O collected in the Table 1. This means that the energy minima of the states of Ce^{3+} - Ce^{4+} pair in which the Ce^{4+} ion is excited into the LMCT states would be located close to the Q_{et}=0 in the Fig. 8. However, in present *ab initio* calculations the energies of LMCT states seem to be largely overestimated due to the choice of the minimal cluster $(CeO_6)^{8-}$, which does not allow for polarization of the neighbors of oxygen ions with the exception of the central Ce ion. Therefore, we estimate the energy position of the bottom of LMCT states from the emission spectra of Sr_2CeO_4 crystal, where the maximum of the emission band is located roughly at 21300 cm^{-1}. This means that in the Fig. 8 the bottom of the states of Ce^{3+} - Ce^{4+} pair in which the Ce^{4+} ion is excited into the LMCT state would coincide at Q_{et} close to zero with the lowest state of $Ce^{3+}(5d^1)$ – Ce^{4+}(GS), where GS denotes "ground state". At the same time the experimental absorption spectrum of Sr_2CeO_4 crystal possesses maximum at roughly 30000 cm^{-1}. This means that the branch of energy curves corresponding to LMCT excitation of Ce^{4+} ion are expected to be in the Fig. 8 for $Q_{et} \approx \pm 0.2$ Å at least few thousands above the lowest $Ce^{3+}(5d^1)$ – Ce^{4+}(GS) state. The direct calculation of the position of O(2p) → Ce(4f) LMCT states performed for larger embedded cluster including second-neighbors of Ce ion and for larger atomic basis set is in progress.

Recently, Seijo and Barandiaran have performed detailed *ab initio* study of the intervalence charge transfer (IVCT) phenomenon within diabatic model for cerium-doped $Cs_2LiLuCl_6$ elpasolite.[42] They have shown that the anomalous emission observed in this system can be attributed to the IVCT luminescence. Furthermore, the IVCT bands are very broad and characterized by large Stokes shift. Consequently, such broad bands may appear in energy regions in which there are no transitions characteristic for a given optically active ion.

In this context we propose that the broadband anti-Stokes white emission observed in Sr_2CeO_4 is realized via the IVCT emission. The concept of the IVCT transitions can be illustrated on the energy diagram of the mixed valence Ce^{3+}-Ce^{4+} pair, as presented in Fig. 8. The two-minima character of the potential energy curves reflects the two energetically equivalent situations of the Ce^{3+}-Ce^{4+} and Ce^{4+}-Ce^{3+} pairs of ions, where the former case is conventionally described as "Ce^{3+} is on the left and Ce^{4+} is on the right side", whereas the latter case states that "Ce^{4+} is on the left and Ce^{3+} is on the right side". The normal electron transfer reaction coordinate Q_{et} in Fig. 8 is determined by the difference between the average Ce-O distances in the CeO_6 clusters containing Ce^{3+} and Ce^{4+}, respectively. Therefore, the two minima of the potential energy curves denoted by solid lines in this figure correspond to two equilibrium geometries of the Ce^{3+}-Ce^{4+} and Ce^{3+}-Ce^{4+} pairs, whereas Q_{et} = 0 refers to the activated complex. Dotted lines indicate the energies of IVCT states corresponding to highly stressed geometries. As mentioned

above, the LIWE emission of Sr_2CeO_4 can be attributed to the IVCT emission transition as follows:

$$[Ce^{3+}\ (5d^1)_{eq}, Ce^{4+}\ (GS)_{eq}] \rightarrow [Ce^{4+}(GS)_{str}, Ce^{3+}(4f^1)_{str}]$$

where "eq" and "str" subscripts denote the "equilibrium" and "stressed" geometries of the CeO_6 clusters in a given state, respectively; GS is the ground state of CeO_6 cluster containing Ce^{4+} ion. It is seen in the Fig. 8 that IVCT emission indeed appears at the energy at which there are no transitions in the separate Ce^{3+} and Ce^{4+} sites. Furthermore, the final state is far from its equilibrium position, i.e. shifted almost 0.4 Å along the Q_{et} coordinate, thus the spectral band corresponding to this transition has to be very broad. The transition energies of IVCT emission seen in the Fig. 8 and defined in Eq. (1) are around 13500 cm^{-1}, which is in relatively good agreement with the position of experimentally observed LIWE band in Sr_2CeO_4. Assuming that our estimations of the position of O(2p) → Ce(4f) LMCT states are correct, their energies are at least few thousands larger than energy of lowest $Ce^{3+}(5d^1)$ – $Ce^{4+}(GS)$ state in the proximity of $Q_{et} \approx \pm 0.2$ Å. This means that the presence of LMCT states should not affect the proposed mechanism of IVCT emission. At the same time, depending on the position on energy scale of the minimum of O(2p) → Ce(4f) LMCT states around $Q_{et} \approx 0$, other mechanisms of LIW emission may appear. The discussion of such mechanism is postponed until the more accurate *ab initio* energies of LMCT states will obtained.

Furthermore, it may happen that the IR multiphoton excitation of the LIWE can be affected by the presence of IVCT states at the positions on energy scale of the virtual states of multiphoton absorption; it is indicated in Fig. 8, where the excitation "1" terminates and excitation "2" starts within the energy range of a bundle of $[Ce^{4+}(GS)_{str}, Ce^{3+}(4f^1)_{str}]$ IVCT states. Once again, such situation was obtained within the *ab initio* calculations performed for $Cs_2LiLuCl_6$:Ce elpasolite.[2] In this case at the equilibrium position of $[Ce^{3+}(4f^1)_{eq}, Ce^{4+}(GS)_{eq}]$ configuration the IVCT states lay in the middle between the ground state and the bottom of $[Ce^{3+}(5d^1)_{eq}, Ce^{4+}(GS)_{eq}]$ configuration. These results support the possibility of the enhancement of multiphoton excitations by the presence of physical intermediate states.

[1] B. A. Saleh, M. A. Teich, Fundamentals of Photonics, John Wiley & Sons, Inc., 1991

[2] L. Seijo and Z. Barandiaran, Intervalence charge transfer luminescence: The anomalous luminescence of ceriumdoped $Cs_2LiLuCl_6$ elpasolite, J. Chem. Phys., 2014,141, 214706.

[3] NIST Computational Chemistry Comparison and Benchmark Database, NIST Standard Reference Database Number 101, Release 17b, September 2015, Editor: Russell D. Johnson III, http://cccbdb.nist.gov/.